Journal of
Materials Chemistry A

PAPER

View Article Online
View Journal | View Issue

Cite this: *J. Mater. Chem. A*, 2023, **11**, 10993

Received 25th February 2023
Accepted 26th April 2023

DOI: 10.1039/d3ta01196h

rsc.li/materials-a

Non-equilibrium plasma-assisted dry reforming of methane over shape-controlled CeO_2 supported ruthenium catalysts†

Md Robayet Ahasan,[a] Md Monir Hossain,[a] Xiang Ding[b] and Ruigang Wang *[a]

In this report, CeO_2 and SiO_2 supported 1 wt% Ru catalysts were synthesized and studied for dry reforming of methane (DRM) by introducing non-thermal plasma (NTP) in a dielectric barrier discharge (DBD) fixed bed reactor. From quadrupole mass spectrometer (QMS) data, it is found that introducing non-thermal plasma in thermo-catalytic DRM promotes higher CH_4 and CO_2 conversion and syngas (CO + H_2) yield than those under thermal catalysis only conditions. According to the H_2-TPR, CO_2-TPD, and CO-TPD profiles, reducible CeO_2 supported Ru catalysts presented better activity compared to their irreducible SiO_2 supported Ru counterparts. For instance, the molar concentrations of CO and H_2 were 16% and 9%, respectively, for plasma-assisted thermo-catalytic DRM at 350 °C, while no apparent conversion was observed at the same temperature for thermo-catalytic DRM. Highly energetic electrons, ions, and radicals under non-equilibrium and non-thermal plasma conditions are considered to contribute to the activation of strong C–H bonds in CH_4 and C–O bonds in CO_2, which significantly improves the CH_4/CO_2 conversion during DRM reaction at low temperatures. At 450 °C, the 1 wt% Ru/CeO_2 nanorods sample showed the highest catalytic activity with 51% CH_4 and 37% CO_2 conversion compared to 1 wt% Ru/CeO_2 nanocubes (40% CH_4 and 30% CO_2). These results clearly indicate that the support shape and reducibility affect the plasma-assisted DRM reaction. This enhanced DRM activity is ascribed to the surface chemistry and defect structures of the CeO_2 nanorods support that can provide active surface facets, higher amounts of mobile oxygen and oxygen vacancy, and other surface defects.

1. Introduction

The production of syngas (mixture of H_2 and CO) for Fischer–Tropsch synthesis (F–T synthesis) using dry reforming of methane (DRM, eqn (1)) represents a growing strategic interest to simultaneously reduce emission of two major greenhouse gases (GHG; CO_2 and CH_4) aiming at limiting global climate change. In fact, the depletion of conventional oil reserves and its environmental consequences have received considerable critical attention with a view to pursuing an alternative roadmap in light of the global energy demand outlook.[1] Among various potential solutions, simultaneous conversion and reuse of two primary GHG (CO_2 and CH_4) *via* catalytic DRM reaction into fuels and value-added chemicals have been considered as one of the attractive strategies.[2] However, due to the sp^3 hybridization, the high C–H bond dissociation energy (434 kJ mol^{-1}) in CH_4 and C=O bond dissociation energy (532 kJ mol^{-1}) in CO_2 require relatively high temperatures to overcome the thermodynamic energy barriers in heterogeneous gas–solid thermal catalysis, which can result in catalyst sintering deactivation and coke formation. For example, thermal catalytic DRM and its syngas production, given in eqn (1), can only be achieved with relatively high temperatures (627–1000 °C).[3,4]

$$CH_4 + CO_2 = 2CO + 2H_2 \tag{1}$$

Besides several lab scale single step conversion methods of CO_2 & CH_4 such as thermo-chemical,[5] electrochemical,[6] and photochemical methods, recently non-thermal plasma reactors have emerged as a powerful platform for DRM conversion. For example, Andersen *et al.* reported that at ambient pressure and temperature, a CO_2 and CH_4 conversion of ~22% and ~33% were achieved, respectively, by introducing non-equilibrium plasma for DRM reaction, while a series of Al_2O_3 supported catalysts can be added to tune the selectivity to H_2 and CO, H_2/CO molar ratio, and selectivity to different hydrocarbons and oxygenates.[7–9]

For plasma-assisted catalytic conversion *via* DRM, various radicals, ions, electrons, and excited intermediate species can be generated by high-energy electrons and ionized gases once the breakdown voltage is reached to form a plasma discharge.

---

[a] Department of Metallurgical and Materials Engineering, The University of Alabama, Tuscaloosa, AL 35487, USA. E-mail: rwang@eng.ua.edu

[b] College of Urban and Environmental Sciences, Peking University, Beijing 100871, China

† Electronic supplementary information (ESI) available. See DOI: https://doi.org/10.1039/d3ta01196h

Thus, the high temperature and pressurized conditions in the thermal catalytic reactor are replaced by highly energetic electrons and abundant radicals/ions in plasma-assisted catalytic reactors. These excited species, typically not available in thermal reactors, are a great advantage of plasma-assisted catalytic reactions that can operate under relatively mild conditions. For example, the chemical reactions in dielectric barrier discharge (DBD) reactors, especially at low temperatures, are mainly governed by electron temperature rather than reactor gas temperature, which controls the bond activation/dissociation and recombination processes of gas molecules. Several experimental and computational studies have suggested that the synergic effect of the combination between the plasma and the catalysts can significantly enhance the gas conversion and product selectivity in DRM.[10–12] Many catalysts have been tested over the last few decades for DRM *via* thermal catalysis, usually operating in the 650–1000 °C temperature range. Noble metals (Rh and Ru) are well known for their high catalytic activities in DRM, but nickel-based catalysts are widely used due to their lower cost but have coke formation issues.[13] For plasma-assisted catalytic DRM using Ru over TiO_2,[14] Al_2O_3,[15] and MgO,[16] it has been demonstrated that plasma has a profound effect on their catalytic activity. In addition, the kinetic studies showed that coordinatively unsaturated Ru surface atoms were more active than those in low-index crystal planes, predominately exposed on large crystallites. Meanwhile, some literature studies reported the stabilization of Ru species over a CeO_2 support by mild oxidative pretreatment.[17,18]

In the supported catalysts, the role of the catalyst support is mainly to provide a high surface area to disperse catalytically active metal or metal oxide clusters for better distribution and thermal stability.[19,20] Among various catalyst supports, CeO_2 has been widely investigated because of its enriched mobile surface oxygen, surface oxygen vacancy, and other surface defects, which contribute to facilitating the catalyst–CeO_2 interaction and gas adsorption (*i.e.*, CO_2 adsorption) due to the reversible reaction between Ce^{4+} and Ce^{3+}. The facile redox Ce^{4+}/Ce^{3+} transition in CeO_{2-x} led to a proliferation of many fundamental catalyst–support interaction studies. The concentration of Ce^{3+} is generally proportional to oxygen vacancy concentration, which illustrates the effectiveness of oxygen exchange between the catalyst and CeO_2 support.[21] In addition, the occupied 4f-orbital electrons of Ce^{3+} ions can promote electronic interaction between reducible CeO_2 and metal nanoparticles.[22] To further improve the oxygen exchange capability of CeO_2, it was discovered that specific shapes of CeO_2 nanoparticles allow a controlled supply of oxygen in a redox-related catalytic reaction such as octahedra, rods, cubes, and spheres.[23–25] For example, the exposed surfaces of CeO_2 nanocubes (CeO_2-NC) with {1 0 0}, CeO_2 nanorods (CeO_2-NR) with {110} and {100} or {1 1 1} and CeO_2 nano-octahedra (CeO_2-NO) with {1 1 1} facets have been most studied for catalytic applications.[8,26–28] Thanks to this unique oxygen storage capacity (OSC) property, reducible CeO_2-based oxides have been utilized in versatile catalytic reactions. On the other hand, irreducible SiO_2 with a high surface area has also been frequently used as oxide catalyst supports, mainly aiming at enhancing the metal cluster dispersion and thermal stability. In general, SiO_2 is considered an inert catalyst support in nature due to the high oxygen vacancy formation energy and low isoelectric point (IEP) of SiO_2 (IEP $\sim$ 2), and it forms weak or no interaction with metal catalyst clusters.[29]

In this work, we report 1 wt% Ru supported on irreducible SiO_2 and reducible CeO_2 with two different morphologies (CeO_2-NR and CeO_2-NC), exposing {110}/{100}/{1 1 1} and {1 0 0} facets respectively to investigate the non-thermal plasma influence as well as the support shape effect on the DRM reaction under non-equilibrium conditions.

2. Experimental section

2.1 Catalyst preparation

2.1.1. Preparation of catalyst supports. The SiO_2 support was synthesized by a modified Stober method from our previous research.[30,31] First, 158 mL absolute ethanol, 7.8 mL NH_4OH (28% NH_3 in H_2O), and 2.8 mL deionized water were introduced in a 250 mL round-bottom flask. The flask was heated to 50 °C under vigorous stirring. Then, 5.8 mL (TEOS 99%) was added dropwise to the solution under vigorous magnetic stirring, and this stirring was continued for another 24 h at 50 °C to achieve complete hydrolysis. The sample was obtained by drying the suspension at 70 °C for 24 h.

CeO_2 nanorods (NR) and CeO_2 nanocubes (NC) were synthesized using a hydrothermal method, according to our previous research methodology.[32–34] For CeO_2 NR, firstly, 8 mL of 6.0 M NaOH (VWR, 99%) solution was added dropwise to 88 mL of 0.1 M $Ce(NO_3)_3 \cdot 6H_2O$ (Acros Organics, 99.5%) solution and appropriately mixed in a 200 mL Teflon liner. The mixture was stirred for approximately 15 s, and the lid of the Teflon liner was closed. The Teflon liner was then put into a stainless-steel autoclave and sealed tightly. The stainless-steel autoclave was heated to 90 °C and kept at this temperature for 48 h. After the hydrothermal reaction, the precipitate materials were washed thoroughly with 500 mL deionized water to remove any residual ions (Na^+, NO_3^-), then washed with 50 mL ethanol to avoid hard agglomeration of the nanoparticles and dried in air at 60 °C for 12 h. The dried sample was collected and ground gently with a mortar and pestle. The preparation of CeO_2 NC followed the same procedure; however, the autoclave was kept at 150 °C instead of 90 °C for 48 h.

2.1.2. Preparation of supported catalysts. 1.0 wt% Ru was loaded onto CeO_2 NR, CeO_2 NC and SiO_2 by impregnating the support powders with an aqueous solution of $Ru(NO)(NO_3)_3$. Specifically, 0.99 g of CeO_2 NR, CeO_2 NC, and SiO_2 powders were put into 100 mL deionized water separately in three 200 mL beakers. $Ru(NO)(NO_3)_3$ (Alfa Aesar) equivalent to 1 wt% Ru was dissolved in each suspension solutions of the support powders. The suspension solutions were mixed properly using magnetic stirring followed by dropwise addition of 0.5 M aqueous solution of ammonium hydroxide ($NH_3 \cdot H_2O$, BDH, 28–30 vol%) to tune the pH value of the suspension to $\sim$9. Then the precipitates were initially heated at 80 °C under stirring (400 rpm) for 4 h. Finally, the precipitates were continuously heated at 100 °C to evaporate water and transferred into a drying oven and kept overnight. To obtain fine powder, a mortar and pestle was used for grinding and left in an air furnace for calcination at a rate of 10 °C min^{-1} up to 350 °C and maintained at this temperature for 5 h. These samples were labeled as 1.0 wt% Ru/CeO_2 NP-o (o refers to the oxidized sample, and NP represents NR or NC) and 1.0 wt% Ru/SiO_2-o. Finally, some of the powder samples were further reduced by heating in a 5% H_2/Ar flow (200 mL min^{-1}) at a rate of 10 °C min^{-1} up to 300 °C and maintained at this temperature for 5 h. After cooling down to room temperature under a H_2 atmosphere, these samples were labeled as 1.0 wt% Ru/CeO_2 NP-r (r refers to the reduced sample) and 1.0 wt% Ru/SiO_2-r.

2.2 Catalyst characterization

Powder X-ray diffraction (XRD) characterization was conducted on a Philips X'Pert MPD diffractometer with a copper Kα radiation source ($\lambda = 0.154$ nm) at 40 kV and 40 mA. The samples were scanned with a scan rate of 0.5° min^{-1} in the 2θ range between 10° and 90°. JADE software was used to determine each catalyst sample's lattice parameters and average crystallite size based on the recorded XRD patterns.

At 77 K, the BET surface area was determined using single-point nitrogen physisorption. A Micromeritics AutoChem II 2920 chemisorption analyzer was used to characterize H_2-temperature programmed reduction (H_2-TPR). The powder samples (85–95 mg) were placed in a quartz U-tube sandwiched between two pieces of quartz wool, then heated at a rate of 10 °C min^{-1} from 30 °C to 900 °C. During the H_2-TPR, the samples were reduced at a flow rate of 50 mL min^{-1} in a 10 vol% H_2–90 vol% Ar gas mixture. A thermal conductivity detector (TCD) was used to monitor the quantity of H_2 uptake during the reduction, which was calibrated using a quantitative reduction of CuO to metallic copper.

Carbon dioxide temperature-programmed desorption (CO_2-TPD) was performed using the same Micromeritics AutoChem II 2920 instrument as for H_2-TPR to investigate the interaction of CO_2 with the catalyst/support surface. First, the quartz wool sandwiched powder sample was put into a quartz U-tube microreactor and heated from room temperature to 400 °C with a He stream (flowrate: 50 mL min^{-1}) to remove residual moisture. After cooling to room temperature, a 10 vol% CO_2–90 vol% He mixture gas was supplied with a flowrate at 50 mL min^{-1} through the sample for 60 min. The sample was then heated up to 900 °C at a linear ramping rate of 10 °C min^{-1} under helium gas. A thermal conductivity detector was used to evaluate the desorption behavior of CO_2 at elevated temperatures.

High-resolution transmission electron microscopy (HRTEM) images were obtained using an FEI Tecnai F20 with an acceleration voltage of 200 kV while a JEOL 7000 FE SEM was used to obtain energy dispersive X-ray spectroscopy data (EDAX system). For the TEM sample preparation, the sample underwent ultrasonic dispersion of the powder in ethanol. One or two drops of the suspension solution were deposited on ultrathin carbon film supported by a 400-mesh copper grid (Ted Pella Inc.) and then dried for 2 h before analysis.

A Kratos Axis Ultra DLD spectrometer using a monochromatic Al Kα ($h\nu = 1486.6$ eV) source under ultra-high vacuum (10^{-10} torr) was used to acquire X-ray photoelectron spectroscopy (XPS) data, and carbon (C) 1s at 284.8 eV was used for calibration of binding energies (BE). The fitting and deconvolution of the spectra were conducted using the CASA XPS software.

Non-destructive Raman characterization of the catalysts was done using a Horiba LabRAM HR 800 Raman spectrometer (equipped with a 100× long working distance objective, NA = 0.60) in the spectral window from 100 to 1200 cm^{-1}. A diode-pumped solid-state (DPSS) laser system (Laser Quantum MPC6000) tuned at $\lambda = 532$ nm was used for excitation. Prior to each analysis, the spectrometer was calibrated using a single crystal Si wafer.

2.3 Catalytic activity measurements

The components of the DBD reactor can be divided into four parts: a gas delivery system, a central quartz reactor tube, an experimental control section, and a flow gas analysis system. Fig. 1 shows a schematic diagram of the whole plasma reactor system. The gas supply system includes three Brooks GF040 Multiflo thermal mass flow controllers (MFC) with <1 s response time, represented by MFC-1, MFC-2, and MFC-3. The flows of Ar, CH_4, and CO_2 with purity >99.99% from Airgas were controlled by these MFCs. A computer interface with a NI card loaded with a home-written MATLAB GUI code was used to control the gas flow of MFCs. Each complete operation of the plasma-assisted DRM reaction consists of a 7 min reduction cycle followed by a 6 min purge with pure Ar gas. During the reduction, the gas mixture of CH_4 and CO_2 flowed with a total flowrate of 350 sccm ($CH_4 : CO_2 = 100 : 250$ sccm), while in the purging step, 100% Ar was flowed to purge the reactor for the subsequent reduction cycle.

For plasma generation, the main reactor includes two concentric quartz tubes placed inside an ATS 3210 split tube furnace that can heat the reactor to 1100 °C and provide an isothermal environment. Three thermocouples TC1, TC2, and TC3 are used to measure the furnace temperature during plasma and thermal DRM reactions. The 2″ length inner quartz tube has an outer diameter (OD) of 1/4″ with an expansion section of 3/8″ inner diameter (ID). This tube links with the supply gas system so that reactive gases flow into the inner tube first. The other side of the inner quartz tube with an open end was placed inside the outer quartz reactor tube. The outer quartz tube has a 1″ OD and is closed at the bottom end. The catalyst sample was dispersed in quartz wool and placed inside the expansion section of the inner quartz tube where the plasma was generated. After entering the inner tube, the reactant gases interact with catalysts and plasma and go through the open end of that tube. The closed outer tube reverses the direction of the gases and flows out to the exhaust. An enlarged schematic of the plasma-catalysis reactor area is shown in Fig. S1.†

The exhaust gas system is analyzed using a quadrupole mass spectrometer (QMS, model: MAX300-EGA from Extrel, 300 ms, 1–250 amu detectability) and a customized tunable diode quantum cascade laser absorption spectroscopy (TDLAS) system. The QMS is connected with a tiny capillary quartz probe

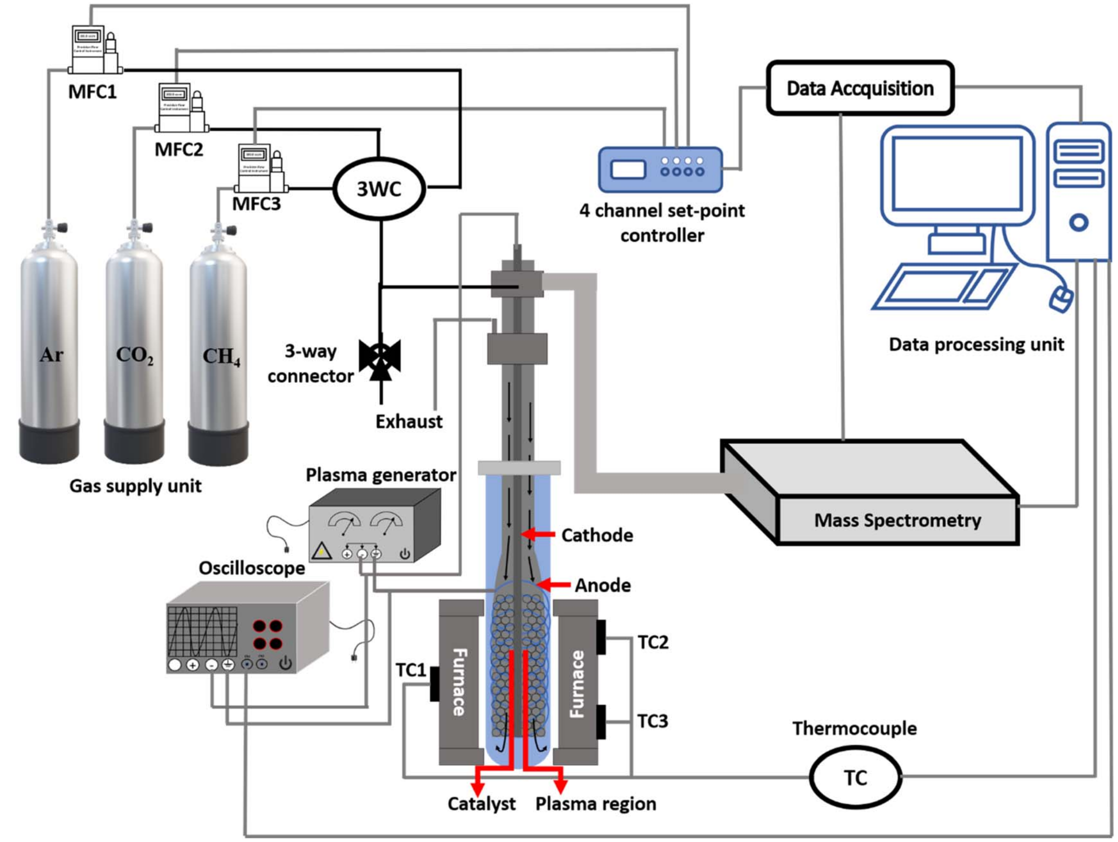

Fig. 1 Schematic of the reactor setup for the plasma-assisted DRM test station. The red color arrows identify the plasma and catalyst regions, as well as the anode and cathode. TC1, TC2, TC3 – thermocouples, 3WC – three-way gas flow controller, and MFC-1, MFC-2, MFC-3 – mass flow controllers.

(0.80 mm OD, 0.53 mm ID) to sample the gases and measure time-resolved species at the probe end location, at the exit of the inlet tube expansion section where the catalyst is placed in plasma. But the TDLAS system is connected at the exhaust line for detecting C-2 based species such as C_2H_2, C_2H_4, and C_2H_6. Before the operation, QMS is calibrated by flowing a known mixture of gases. All gases (CO_2, CO, H_2, CH_4, Ar, O_2) flowed simultaneously for calibration. Typically, increasing the gas flow rate decreases the gas residence time in the reaction region, while the QMS sensitivity to species measurements also decreases due to the large dilution of H_2 by the balance gas Ar.[35,36] Thus, a lower flow rate increases gas residence time and makes it comparable to reaction time constants (5–10 s), and therefore we choose an optimum total volume flow rate of 350 sccm for our experiments. According to a calculation by dividing the reaction region volume by the gas volume flow rate at the reactor temperature, the gas residence time at the catalyst and plasma regions is <0.5 s. The expanded part of the inner quartz reactor tube contains two coaxial electrodes. One electrode is placed at the center of the inner inlet tube inside a 0.063 ID ceramic tube as a dielectric barrier. Another is placed on the outside of the expansion section spirally surrounding the tube, giving rise to Dielectric Barrier Discharge (DBD) which produces non-equilibrium plasma. Those two electrodes are connected to a plasma driver (PVM500-2500 from https://www.amazing1.com) integrated with a voltage regulator (1–40 kV) with a 20–70 kHz discharge frequency to generate the plasma.

In our experiment, the total flow rate of the gas mixture was maintained at 350 sccm (standard cubic centimeter min^{-1}) during the reduction step. The mixture of gases contains CH_4 (100 sccm or 28.6 vol%) and CO_2 (250 sccm or 71.4 vol%).

In previous reports,[37,38] it was claimed that the metastable O species could accelerate the dissociation of CH_4 and promote CH_4 conversion. In this project, in the supplied gases of DRM reaction, CO_2 is the only source of oxygen. To reduce the CH_x recombination and the formation of byproducts, excess CO_2 supply was used in this project (CH_4: 100 sccm or 28.6 vol% and CO_2: 250 sccm or 71.4 vol%). The average gas velocity is ~6.48 cm s^{-1} at 25 °C in the reactor environment. The measured plasma power was 10.2 to 13.6 W during the reduction cycle (DRM reaction). This variation possibly happened due to gas breakdown voltage and concentration.[38] Similarly, Yabe *et al.*[39] also reported this power variation for different Ni/M–ZrO_2 catalysts. It should be noted that a portion of plasma power is lost by heating the cable, electrodes, and reactor wall from the applied plasma power. For instance, Nozaki *et al.*[40] reported a maximum of 25% power consumption for increasing gas temperature theoretically, while it was 15% in practical experiments. Only Ar was supplied during the purging step at a flowrate of 350 sccm. All experiments were conducted at 1 atm pressure and in the temperature range of 150–450 °C. A single periodic operation consists of 6 min purge and a 7 min reduction step.

2.4 Performance parameters

The conversion rate is defined as the molar ratio of how much the reactant is converted according to the input. The yield of a reaction is calculated as the ratio of the desired product formed (in moles) to the total amount that could have been made (if the yield of the limiting reactant is 100% and no side reaction occurs), while selectivity of a reaction is the ratio of the desired product formed (in moles) to the undesired product formed (in moles). The formulae of CH_4 and CO_2 conversion and product (H_2 and CO) selectivity and yield for a DRM reaction are given below:

$$C_{\mathrm{CH_4}} = \frac{\text{moles of CH}_4\text{ converted}}{\text{moles of CH}_4\text{ input}} \times 100\% \tag{2}$$

$$C_{\mathrm{CO_2}} = \frac{\text{moles of CO}_2\text{ converted}}{\text{moles of CO}_2\text{ input}} \times 100\% \tag{3}$$

$$Y_{\mathrm{H_2}}(\%) = \frac{\text{moles of H}_2\text{ produced}}{2 \times \text{moles of CH}_4\text{ input}} \times 100\% \tag{4}$$

$$Y_{\mathrm{CO}}(\%) = \frac{\text{moles of CO produced}}{\text{moles of CH}_4\text{ input} + \text{moles of CO}_2\text{ input}} \times 100\% \tag{5}$$

$$S_{\mathrm{H_2}}(\%) = \frac{\text{moles of H}_2\text{ produced}}{2 \times \text{moles of CH}_4\text{ converted}} \times 100\% \tag{6}$$

$$S_{\mathrm{CO}}(\%) = \frac{\text{moles of CO produced}}{\text{moles of CH}_4\text{ converted} + \text{moles of CO}_2\text{ converted}} \times 100\% \tag{7}$$

3. Results and discussion

3.1 Powder X-ray diffraction and TEM/EDX analysis

Fig. 2 shows the XRD patterns of CeO_2 and amorphous SiO_2 supported 1 wt% Ru catalysts after the oxidation (Fig. 2a) and reduction (Fig. 2b) treatments. The XRD patterns of CeO_2 NR and NC match well with the face-centered cubic fluorite structure of ceria (JCPDS #34-0394 and space group *Fm*3*m*). The XRD pattern of SiO_2 “aligns” with the standard JCPDS card of amorphous SiO_2 (PDF #00-038-0360). Three intense diffraction peaks appeared at 2θ of 28.6, 47.5, and 56.4, corresponding to the crystal planes of CeO_2 (111), (220), and (311), which confirmed that CeO_2 NR and NC with impregnated RuO_x maintained their fluorite-type structures after calcination at 350 °C for 5 h in air and H_2 reduction treatment at 300 °C for 5 h.[41] The diffraction peaks for CeO_2 NR and CeO_2 NC are in similar positions. However, their relative intensities and sharpness indicate that CeO_2 NR has a smaller crystallite size and/or smaller crystalline domains compared to those of CeO_2 NC. For both oxidized and reduced 1 wt% Ru/CeO_2 NR and NC, no apparent diffraction peaks were detected for either RuO or Ru. Possible explanations for the absence of RuO_x ($0 \leq x \leq 1$) species are (a) RuO_x diffusion into the CeO_2 lattice or formation of Ru–O–Ce solid solution, (b) highly dispersed RuO_x on CeO_2 and (c) low RuO_x loading (1 wt%).[42] Meanwhile, the XPS and *in situ* DRIFTS data revealed the presence of RuO_x species on both CeO_2 NR and NC.

The estimated crystallite sizes of SiO_2 and CeO_2 supported RuO_x samples are enlisted in Table S1† using the Scherrer equation from XRD peak analysis. Besides, the EDS line spectrum and elemental mapping are also presented in Fig. 3, suggesting a uniform distribution of RuO_x over CeO_2. On the other hand, after calcination and reduction treatment of 1 wt% Ru/SiO_2, as shown in Fig. 2, the XRD profiles show the peaks of RuO_2 for the calcined sample and metallic Ru for the reduced sample. The main RuO_2 peaks are observed at $2\theta = 28.2$, 35.3, and 54.6, while metallic Ru peaks are observed at 42.3 and 44 with relatively low peak intensity.

3.2 H_2-temperature programmed reduction (H_2-TPR)

The H_2-TPR profiles of the prepared catalysts can be utilized to investigate oxygen release capacity or H_2 consumption and identify possible surface metal/oxide species and the nature of active sites. As shown in Fig. 4, the H_2-TPR signals show a few hydrogen consumption peaks corresponding to the reduction of surface oxygen (O_s) and bulk oxygen (O_b).[33] All of the oxidized and reduced CeO_2 samples display three main reduction peaks at less than 200 °C, 200–500 °C and greater than 500 °C.[43] In the region below 200 °C, 1 wt% Ru/CeO_2 NR-o presents two reduction peaks at 105 °C and 129 °C resulting from multiple oxidation states of RuO_x due to the interaction between RuO_x and CeO_2.[43] Two similar peaks (surface oxygen reduction peaks) also appear at 115 °C and 158 °C for 1 wt% Ru/CeO_2 NC-o. Notably, the reduction peaks of 1 wt% Ru/CeO_2 NR-o appear at slightly lower temperatures than those of 1 wt% Ru/CeO_2 NC-o. The latter two regions of the oxidized CeO_2 samples have significantly lower intensity and are barely observable due to a higher amount of H_2 consumption below 200 °C and the corresponding scaling factor. After the reduction treatment of the catalysts, there is an increase in BET surface area for each catalyst. This is due to the redispersion of partially reduced RuO_x species over CeO_2 supports. For example, Fernández *et al.*[44] reported the disaggregation and transformation of large RuO_2 to small round shape Ru crystallites after reduction treatment. The H_2-TPR profiles of the reduced sample are shown in Fig. 4(b). After the reduction treatment of two CeO_2 samples, three hydrogen consumption peaks were also observed but with a slightly lower reduction temperature. For example, the O_s peak shifted from 105 °C for 1 wt% Ru/CeO_2 NR-o to 82 °C for 1 wt% Ru/CeO_2 NR-r while a similar peak shifted from 115 °C for 1 wt% Ru/CeO_2 NC-o to 67 °C for 1 wt% Ru/CeO_2 NC-r. The BET surface area, crystal size, total H_2 consumption and reduction temperature data are shown in Table S1.† The pore size distribution and total pore volume of

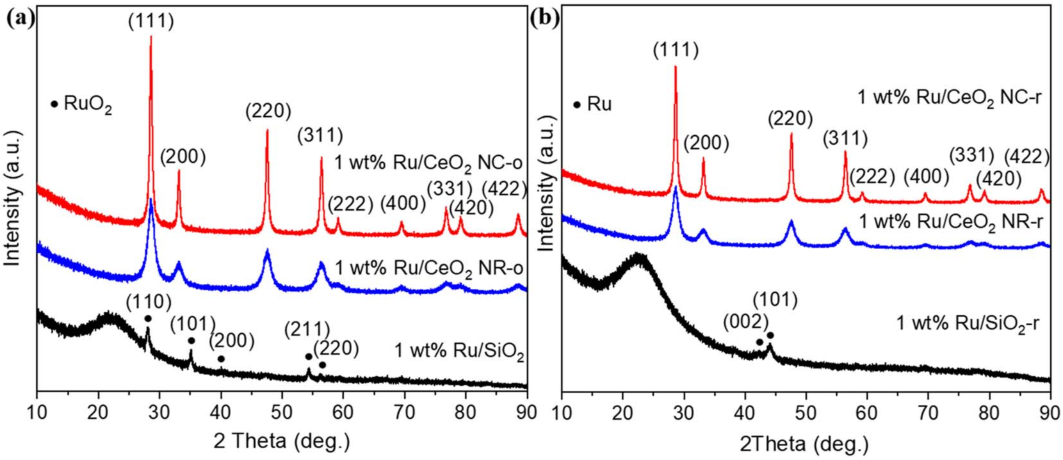

Fig. 2 XRD patterns of 1 wt% Ru/SiO_2, 1 wt% Ru/CeO_2 NR, and 1 wt% Ru/CeO_2 NC for (a) the oxidized and (b) reduced samples.

both 1 wt% Ru/CeO_2 NC and 1 wt% Ru/CeO_2 NR catalysts are shown in Fig. S2.†

The shift of these hydrogen consumption peaks after a reduction treatment are attributed to the activation of Ru catalysts.[27,45] Because after reduction treatment, metallic Ru can easily donate electrons and surround the Ru-oxide support interface by electron-enriched oxygen ions.[42] These "donated" electrons can be easily released, are involved in bond breaking, and promote gas conversion reactions with activated CO_2 and CH_4 species. The H_2-TPR profile of 1 wt% Ru/SiO_2-o showed one low-intensity peak at 146 °C, which shifted to 57 °C for 1 wt% Ru/SiO_2-r. The reduction peaks at 517 °C and 532 °C for Ru/SiO_2 present relatively low intensity compared to Ru/CeO_2. These reduction peaks are possibly related to (1) the mixed RuO_2–SiO_2 phases formed; (2) decomposition of precursors; and (3) the reduction of RuO_2.[46,47]

3.3 CO_2-temperature programmed desorption (CO_2-TPD)

To better understand the CO_2 adsorption–desorption behavior and nature of different basic sites on the prepared oxidized and reduced catalysts, CO_2-TPD measurements were carried out as the DRM reaction is initiated by an acid–base interaction, where CO_2 acts as an acid towards the catalyst with basic properties. Thus, the adsorption and activation of acidic CO_2 depend on the base catalyst's surface, which will determine the overall conversion and catalyst stability. The CO_2-TPD profiles in Fig. 5(a–c) demonstrate the surface basicity of SiO_2, CeO_2 NR, and CeO_2 NC supported RuO_x, respectively. The typical CO_2-TPD profile consists of contributions from three fundamental group classes that corresponds to weak Brønsted basic sites (*e.g.*, surface OH groups), Lewis acid–base sites of medium strength, and low-coordination oxygen anions as strong basic

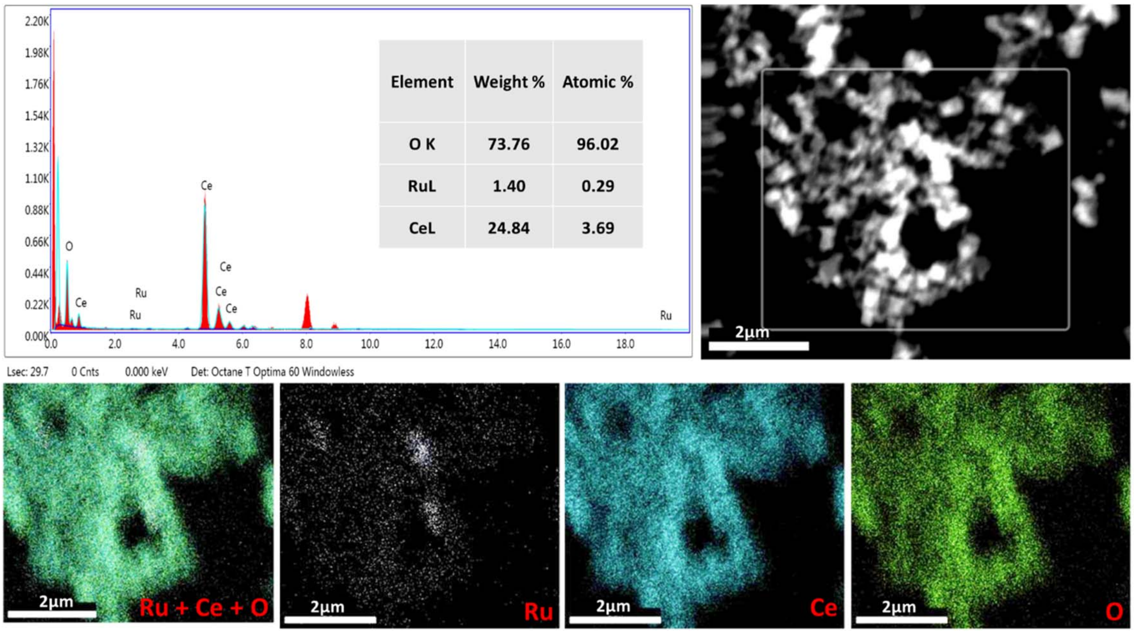

Element	Weight %	Atomic %
O K	73.76	96.02
RuL	1.40	0.29
CeL	24.84	3.69

Fig. 3 EDS line spectrum and elemental mapping of 1 wt% Ru/CeO_2 NC-r catalyst.

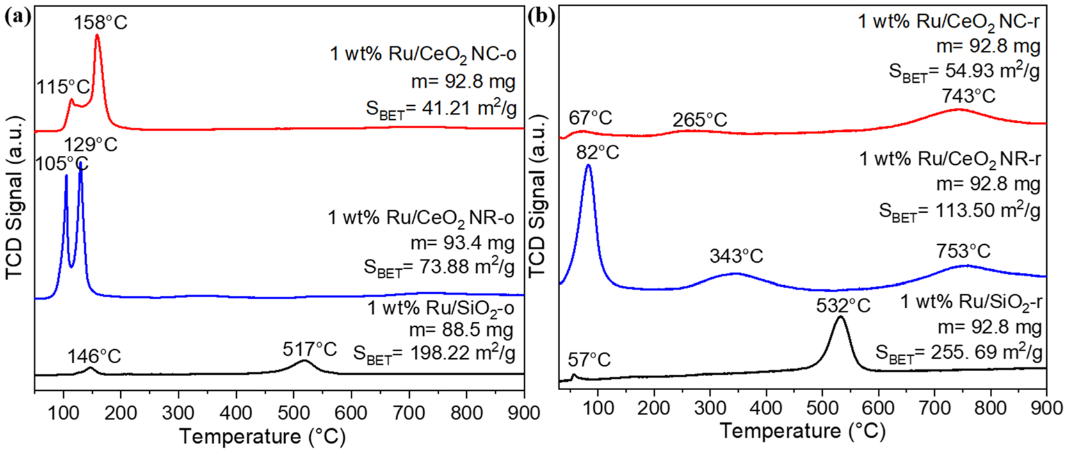

Fig. 4 H_2-TPR profiles of CeO_2 NP and SiO_2 supported RuO_x catalysts after (a) oxidation treatment and (b) reduction treatment.

sites, respectively.[48] These three classes of basic sites appeared at three temperature regions, 50–150, 150–250, and >250 °C.[49] The CO_2-TPD profiles of 1 wt% Ru/SiO_2-o and 1 wt% Ru/SiO_2-r consist of three desorption peaks from 300 °C to 900 °C. These three peaks appeared at 395 °C to 425 °C, 535 °C to 555 °C and 790 °C to 860 °C corresponding to CO_2 desorption from strong basic sites.[50] Thus, no weak or medium CO_2 desorption happened for Ru–SiO_2 catalysts due to poor interactions between Ru and SiO_2.

The desorption peaks of the reduced sample appeared at a slightly lower temperature than those of the oxidized catalyst due to the activation of Ru particles by the H_2 reduction treatment. The H_2 reduction treatment typically plays roles in catalyst activation including: (a) the reduction of RuO_x to metallic Ru which can lead to an enhanced reaction rate of CH_4 adsorption and decomposition; (b) creating oxygen vacancies due to the reduction treatment which promotes CO_2 activation and C–O bond cleavage; (c) removing the surface water/CO_2 which makes the surface more basic. The effects of the reduction treatment of CeO_2 NR and NC supported 1 wt% Ru can be clearly seen in Fig. 5(b) and (c). Both oxidized and reduced 1 wt% Ru/CeO_2 NR and 1 wt% Ru/CeO_2 NC present three CO_2 desorption peaks at 150–215 °C, 380–410 °C and 700–850 °C, respectively. Here, the weak and moderate adsorptions in the low temperature range correspond to the formation of bridged and bidentate carbonates in the 50–150 °C and 150–250 °C regions. The high-temperature peaks at greater than 250 °C are attributed to the formation of carboxylate and monodentate carbonates with stronger CO_2 adsorption.[51] Both of 1 wt% Ru/CeO_2 NP-o samples showed low-temperature CO_2 desorption peaks, while the reduced samples showed broader desorption peaks. This indicates that a reduced catalyst allowed a higher amount of CO_2 desorption at low temperatures, which can promote the DRM reaction. According to the literature,[52] broad

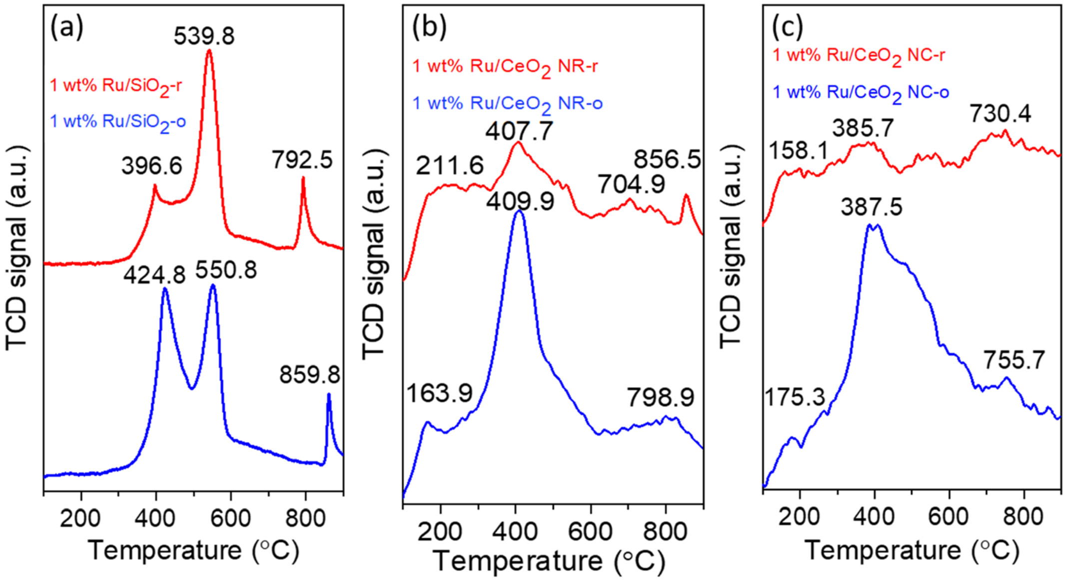

Fig. 5 CO_2-TPD profiles of the oxidized and reduced (a) SiO_2, (b) CeO_2 NR, and (c) CeO_2 NC supported RuO_x catalysts.

desorption CO_2 peaks suggest a higher amount of basic sites, which can reduce the coking or deactivation of the catalyst by the reaction: $CO_2 + C = 2CO$. CO_2 adsorption on weak and moderate basic sites promotes the formation of active carbonate species on the metal–support interface of the catalysts, while CO_2 adsorption on strong basic sites could lead to direct decomposition of CH_4 and aggregation of carbon on active metal catalysts. These active carbonate species can interact with CH_4 and produce CO between the interaction of O from carbonate species and C from CH_4 decomposition. Li *et al.*[53] reported that CO_2 adsorption on medium-strength basic sites leads to easy activation of CO_2 compared to that on strong basic sites. The desorption peaks of the reduced sample shifted to a lower temperature compared to oxidized 1 wt% Ru/CeO_2 NP which indicates that loading of active Ru promotes the formation of weak and medium strength basic sites and CO_2 derived species and accelerates DRM. From Fig. 5(b) and (c), it seems that the shape effect of the CeO_2 support on CO_2 desorption is negligible from CO_2-TPD.

3.4 X-ray photoelectron spectroscopy (XPS)

In order to understand the valence states and surface chemical composition of the oxidized and reduced catalysts, XPS characterization was executed. Fig. 6(a–c) show the XPS spectra of the 3d orbital of Ru and Ce and 1s orbital of O. In the case of 1 wt% Ru/CeO_2 NR-o, RuO_x is analyzed based on the 3d orbital of Ru, which gives intense peaks but which overlap with C 1s peaks. The deconvolution of the Ru 3d core-level spectrum exhibits four different components centered at 280.61 eV, 281.81 eV, 285.21 eV, and 286.01 eV. These peaks are assigned to Ru^{n+} $3d_{5/2}$ ($4 < n < 6$), Ru^{6+} $3d_{5/2}$, Ru^{n+} $3d_{3/2}$ ($4 < n < 6$) and Ru^{6+} $3d_{3/2}$ respectively. The peaks observed at 283.71 eV and 287.81 eV could be C 1s peaks. For the reduced 1 wt% Ru/CeO_2 NR, four similar peaks are also observed with slightly lower binding energy. From these peaks, two deconvolution peaks centered at 281.31 eV and 285.61 eV still showed Ru^{n+} ($4 < n < 6$) species, while the two remaining peaks with binding energy 280.31 eV and 284.81 eV are assigned to spin–orbit coupling of Ru^{4+} $3d_{5/2}$ and Ru^{4+} $3d_{3/2}$ respectively.[27]

The existence of Ru^{n+} species suggests possible electron transfer from RuO_x to CeO_{2-x}, which promotes the formation of Ru–O–Ce solid solution or increases oxygen vacancy concentration.[54] Fig. 6(c) shows the XPS spectrum of the 1s orbital of O for two CeO_2 NR samples. The broad peak of O 1s for oxidized and reduced CeO_2 NR supported RuO_x is evaluated by fitting into two components: lattice oxygen (O_L) and oxygen vacancy (O_V) as well as chemisorbed oxygen (O_C) centered at 530.11 eV and 531.91 eV, respectively. The relative content of these two oxygen species was calculated using the following formula: $O_v/(O_v + O_L)$. The relative oxygen contents are similar, with the values of 50.1% and 49.5% for 1 wt% Ru/CeO_2 NR-o and 1 wt% Ru/CeO_2 NR-r, respectively. For the XPS spectra of Ce 3d shown in Fig. 6(b), there are eight peaks from four pairs of Ce $3d_{3/2}$ and Ce $3d_{5/2}$, which correspond to Ce^{3+} and Ce^{4+} ions. These peaks labeled as U°, U′, U″ and U‴ belong to Ce $3d_{3/2}$, and the peaks labeled as V°, V′, V″ and V‴ are assigned to Ce $3d_{5/2}$. The peaks located at 883.81 eV (V°) and 901.41 eV (U°) are attributed to the concentration of Ce^{3+} ions from Ce $3d_{5/2}$ and Ce $3d_{3/2}$, respectively. The remaining peaks appearing at 882.81 eV, 889.51 eV, 898.91 eV, 901.41 eV, 908.21 eV, and 917.31 eV labeled as V′, V″, V‴, U′, U″ and U‴ represent the concentration of Ce^{4+} ions. The

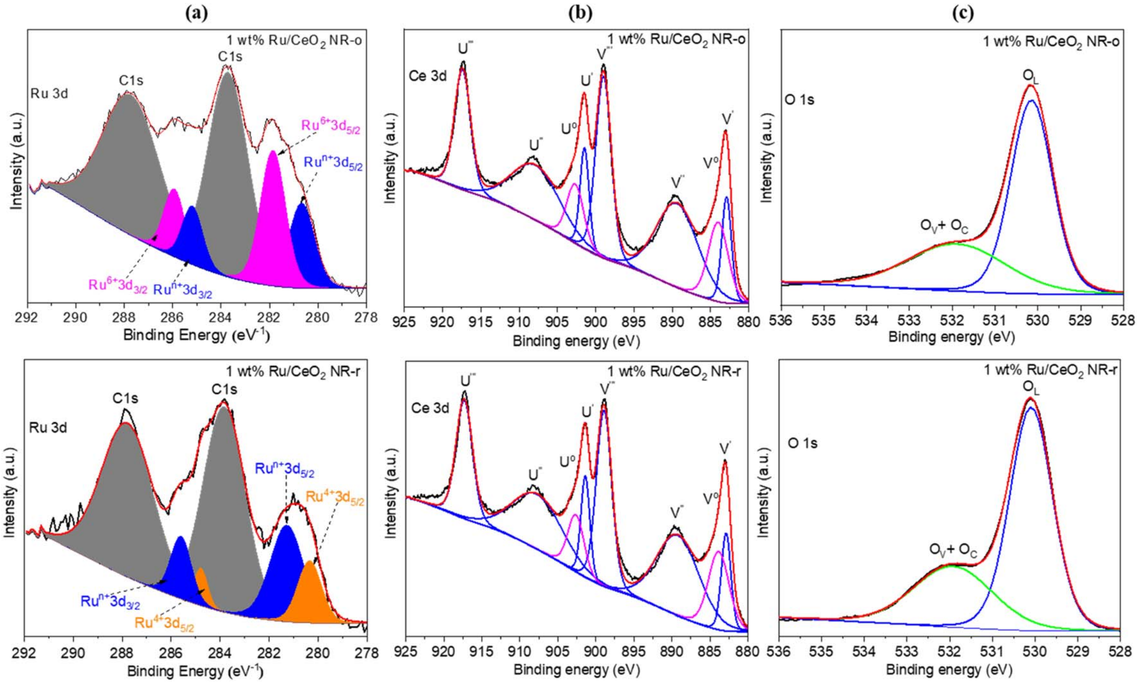

Fig. 6 XPS spectra of the 1 wt% Ru/CeO_2 NR samples after the oxidation (upper row) and reduction treatments (bottom row) for (a) Ru 3d, (b) Ce 3d, and (c) O 1s. O_v and O_c refer to the oxygen vacancy and chemisorbed oxygen, respectively.

relative concentration of Ce^{3+} ions can be calculated by integrating each peak area using the equation below:

$$[\mathrm{Ce}^{3+}] = \frac{A_{\mathrm{u}^\circ} + A_{\mathrm{v}^\circ}}{A_{\mathrm{u}^\circ} + A_{\mathrm{v}^\circ} + A_{\mathrm{u}'} + A_{\mathrm{u}''} + A_{\mathrm{u}'''} + A_{\mathrm{v}'} + A_{\mathrm{v}''} + A_{\mathrm{v}'''}} \quad (8)$$

The concentration of Ce^{3+} was 26.54% and 23.24% for the reduced and oxidized 1 wt% Ru/CeO_2 NR catalysts, respectively. One of the main reasons for the slight difference in Ce^{3+} concentrations is the reduction treatment temperature. We reduced the treatment temperature of each catalyst to 300 °C in a H_2 environment. A valid reason for this low reduction treatment temperature is to maintain the shape of the CeO_2 NP because CeO_2 shape is highly influenced by temperature. As shown in Fig. S3,† the initial reduction for CeO_2 NR started at around 350 °C. Thus, besides the small reduction of CeO_2, RuO_2 is mainly reduced by the reduction treatment and leads to an increase in oxygen vacancy concentration. From oxidized and reduced XPS characterization data of 1 wt% Ru/CeO_2 NR, it is apparently clear that partially reduced Ru^{n+} ions increase significantly along with the slight increase of Ce^{3+} ion concentration after reduction treatment. The formation of Ce^{3+} ions is believed to relate to the available oxygen vacancy, and such undercoordinated Ce^{3+} ions due to Ru doping on the surface of a small CeO_2 crystal could result in lattice distortion.[55]

3.5 Transmission electron microscopy (TEM)

Fig. 7 displays the low and high-magnification TEM images of CeO_2 NR and NC supported RuO_x catalysts. Both rod and cube-shaped CeO_2 supports maintained their initial morphology after Ru loading, calcination, and reduction treatment. The length and diameter of CeO_2 NR for the reduced sample are in the range of 50 to 80 nm and 5 to 10 nm, respectively. The cube-shaped CeO_2 has an approximate length of 20 to 40 nm. The Ru crystallites are hard to detect due to their smaller size and low doping amount (1 wt%). However, Fig. 3 indicated the presence of Ru by EDS elemental mapping. The HRTEM images also demonstrate the rough surface of CeO_2 NR, which indicates the presence of lattice distortion, lattice defects, and voids, among many other surface defects. The exposed crystal facets of CeO_2 NC are (100) lattice fringes, while CeO_2 NR possesses a mixture of (111), (100), and (011) lattice fringes with the corresponding *d*-spacings of 3.08–3.16 Å, 2.7 Å and 1.9 Å, respectively, observed from the HRTEM images.

4. Performance test

Fig. 8 shows the molar fraction of CO_2, CH_4, CO, and H_2 obtained from Extrel QMS for DRM at seven different temperatures from 150 °C to 450 °C. This "plasma-off–plasma-on" experiment was designed to understand the synergistic effect of plasma and thermal catalysis in DRM. The plasma was introduced for seven minutes, initiating in the 6th minute and stopping at the 12th minute, followed by a 5 minute thermal only DRM reaction. The effect of introducing plasma in a thermal DRM is very clear from Fig. 8, where two different colors indicate thermal and plasma + thermal regions. For example, at 150 °C, initially, there were "no detectable" CO and H_2 gases for five minutes in the thermal catalysis region. Upon the initiation of plasma at the 6th minute, CO (red line) and H_2

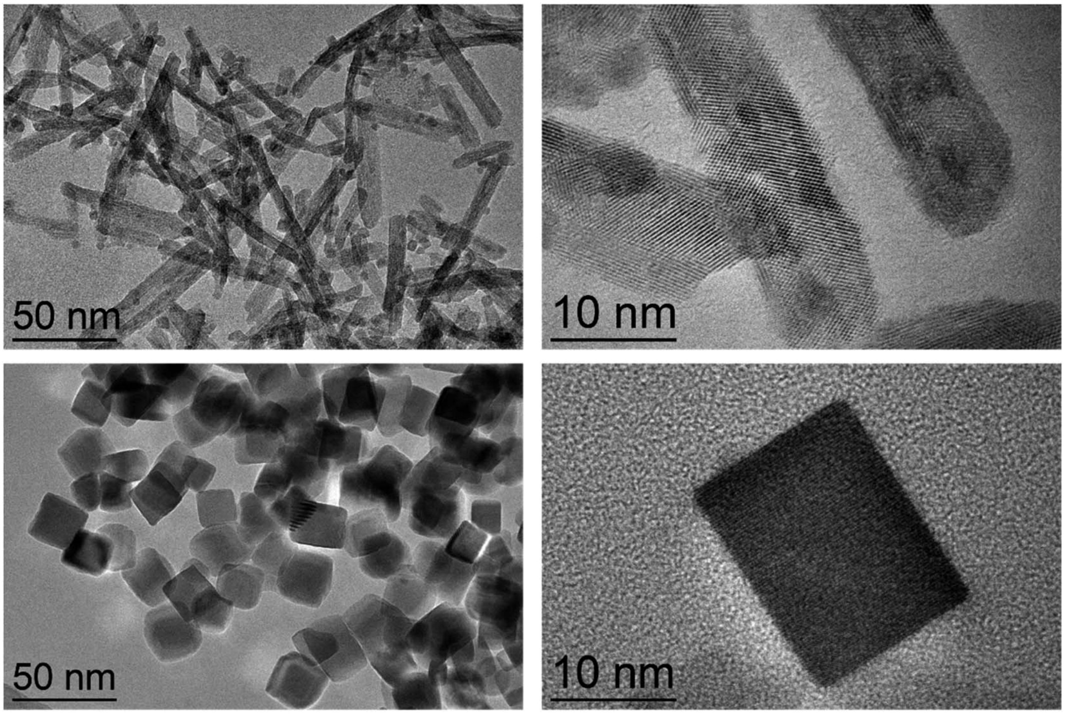

Fig. 7 HRTEM images of 1 wt% Ru/CeO_2 NR-r and 1 wt% Ru/CeO_2 NC-r.

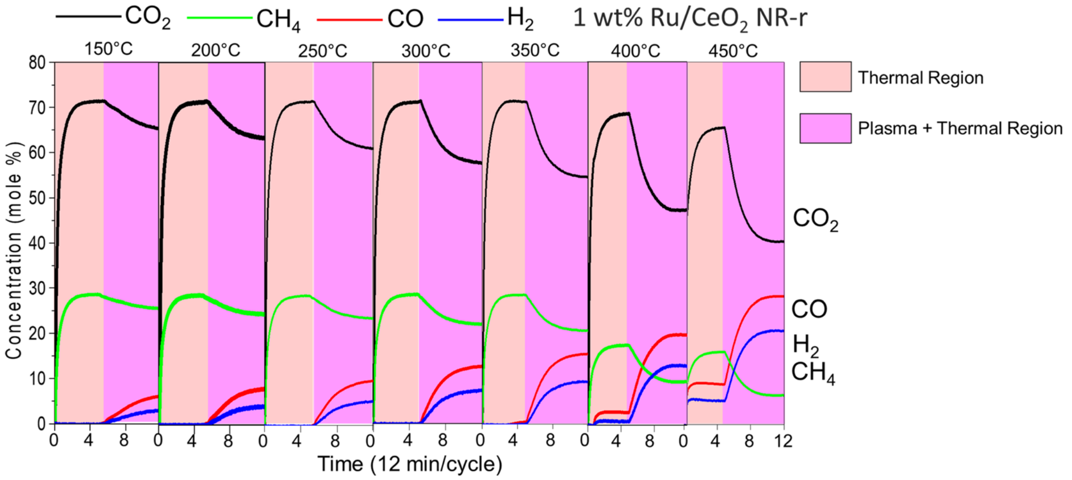

Fig. 8 Measured time-resolved species mole fraction for thermal and thermal + plasma regions from 150 °C to 450 °C, 1 atm pressure (5 min for thermal catalysis only and 7 min for thermal + plasma catalysis) (catalyst wt: ~200 mg, power: 10.2 to 13.6 W, frequency: 20 kHz, flowrate: CO_2: 250 sccm and CH_4: 100 sccm).

(blue line) gases were clearly observed with a sudden decrease in mole concentration of supplied CO_2 (black line) and CH_4 (green line). For the thermal catalysis region at 150 °C, the mole percentage of both CO and H_2 was "zero", which changed to 7% and 3%, respectively, when plasma was introduced. In this project, we utilized both a thermopile infrared array sensor and infrared thermometer to measure the surface temperature of the catalysts during plasma-assisted catalytic DRM reaction. It should be noted that the measured surface temperature of the catalysts is reasonably close (10–40 °C) to the reactor temperature as shown in Fig. S4.† There was "no detectable" CO and H_2 up to 350 °C for thermally driven DRM. Thus, in the temperature range from 150 °C to 350 °C in the plasma + thermal region, the conversion of CH_4 and CO_2 gradually increased, which is due to the introduction of non-thermal plasma. The mole percentage of CO and H_2 increased from 7% to 16% and 3% to 9% from 150 °C to 350 °C in the plasma + thermal region. This indicates that the introduction of plasma plays a crucial role in initiating and promoting low-temperature DRM to produce syngas. For 400 °C and 450 °C, CO and H_2 concentrations were less than 10% for thermal DRM. For example, for the thermal region at 450 °C, CO and H_2 concentrations were 9% and 5%. However, for the plasma + thermal region at 450 °C, these concentrations were 28% and 21% for CO and H_2, respectively, which are significantly higher than those in the thermal-only DRM regions. The CO and H_2 molar concentrations *vs.* time at temperature between 150 °C and 450 °C is shown in Fig. S5.† At low temperatures, it takes time for the reaction to reach equilibrium, whereas at high temperatures, it stabilizes rapidly. In Fig. S6,† a 10 min plasma-assisted reduction cycle for the 1 wt% Ru/CeO_2 NR-r catalyst at 250 °C is shown, which clearly illustrates that there was no noticeable change from MS in the molar concentration of CO_2, CH_4, CO, or H_2 after 7 minutes. According to our Quantum Cascade Laser (QCL) absorption system, a very tiny amount of C_2H_6 or ethane was detected during plasma-assisted DRM as shown in Fig. S7.†

Fig. 9 shows the conversion of DRM reaction with only plasma, plasma-assisted only support, plasma-assisted catalyst, and thermal catalysts at 450 °C, 400 °C, and 350 °C. It is noticeable that plasma-assisted DRM is extraordinarily high compared to thermally driven DRM. Plasma and catalyst synergism highly enhanced the DRM conversion close to 51% and 37% for CH_4 and CO_2, respectively, at 450 °C. However, DRM conversion with only plasma and plasma-assisted only support was less than 5% for both CH_4 and CO_2.

All the CO_2, CH_4, CO, and H_2 species profiles acquired from QMS were time integrated to obtain the total amounts of the products at each temperature which were later used for quantitative calculation of conversion, selectivity, and yield shown in Fig. 10 and 11.

The conversion of the reactants CH_4 and CO_2 under thermal only and plasma + thermal conditions is presented in Fig. 10(a–d) in the temperature range 150 °C to 450 °C for two catalysts: 1 wt% Ru/CeO_2 NR and 1 wt% Ru/CeO_2 NC. These experimental results were obtained from the reaction conditions where the catalysts were placed in the plasma zone with a constant temperature zone of the furnace. In this case, plasma was in direct contact with the catalyst, and the furnace temperature seriously influenced the plasma zone. It is important to mention that no conversion occurred in thermal DRM till 250 °C for 1 wt% Ru/CeO_2 NC and 300 °C for 1 wt% Ru/CeO_2 NR, which is consistent with the observations in the literature due to the endothermic nature of DRM reaction.[56] Typically for thermally driven DRM, the conversion of CH_4 and CO_2 was observed at operating temperatures higher than 300 °C.[50] For thermally driven DRM, CH_4 conversion percentage is typically lower compared to CO_2 conversion, which may be a result of the simultaneous reverse water-gas shift (RWGS) reaction ($CO_2 + H_2 = CO + H_2O$).[57] The conversion trends of CH_4 and CO_2 over 1 wt% Ru/CeO_2 NC and 1 wt% Ru/CeO_2 NR samples are similar, and the conversion percentage of 1 wt% Ru/CeO_2 NC was "even" higher than for 1 wt% Ru/CeO_2 NR under thermally driven

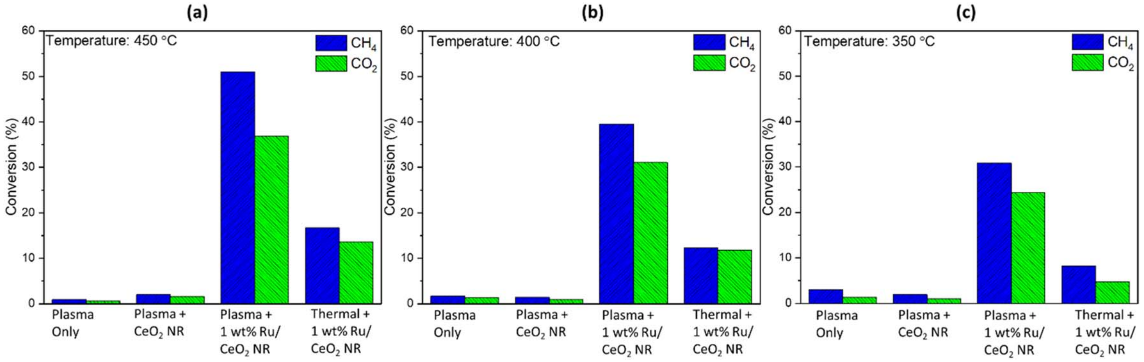

Fig. 9 CH_4 and CO_2 conversion with only plasma, plasma + CeO_2 NR, plasma + 1 wt% Ru/CeO_2 NR and thermal + 1 wt%/CeO_2 NR at (a) 450 °C, (b) 400 °C and (c) 350 °C (catalyst wt: ~200 mg, power: 10.2 to 13.6 W, frequency: 20 kHz, flowrate: CO_2: 250 sccm and CH_4: 100 sccm).

DRM. For example, at 450 °C, CO_2 conversion was 17% for 1 wt% Ru/CeO_2 NC, which is 3% greater than for 1 wt% Ru/CeO_2 NR (14%). In similar work, Zhou *et al.*[58] reported that the reaction rate of Ru dispersed on CeO_2 NC was higher than that of Ru dispersed on CeO_2 NR. Although kinetic modeling indicates similar turnover frequency (TOF) for CeO_2 NC and CeO_2 NR based on surface-oxygen vacancies ($2.67–2.91 \times 10^{-4}$ s^{-1}) and activation energies (72.9–76.4 kJ mol^{-1}), the higher performance of thermally driven DRM over 1 wt% Ru/CeO_2 NC is rooted in oxygen vacancy concentration at the RuO_x–CeO_2 interface. Compared to thermally driven DRM, Fig. 10(a–d) show that reaction conversion for both CH_4 and CO_2 for plasma-assisted DRM is extraordinarily high. It is clear that the trigger temperature of plasma-assisted thermo-catalytic DRM was at

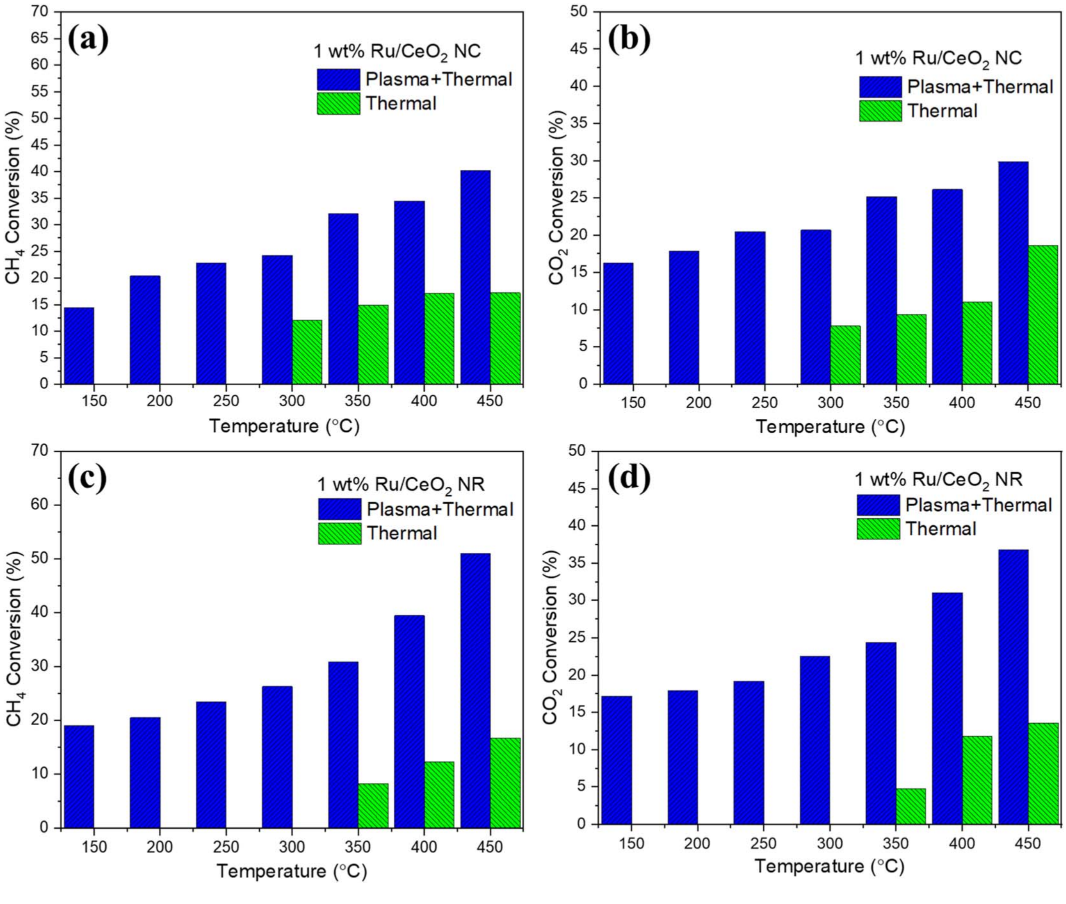

Fig. 10 (a) CH_4 and (b) CO_2 conversion of 1 wt% Ru/CeO_2 NC; (c) CH_4 and (d) CO_2 conversion of 1 wt% Ru/CeO_2 NR from 150 °C to 450 °C under thermal and thermal + plasma conditions (catalyst wt: ~200 mg, power: 10.2 to 13.6 W, frequency: 20 kHz, flowrate: CO_2: 250 sccm and CH_4: 100 sccm).

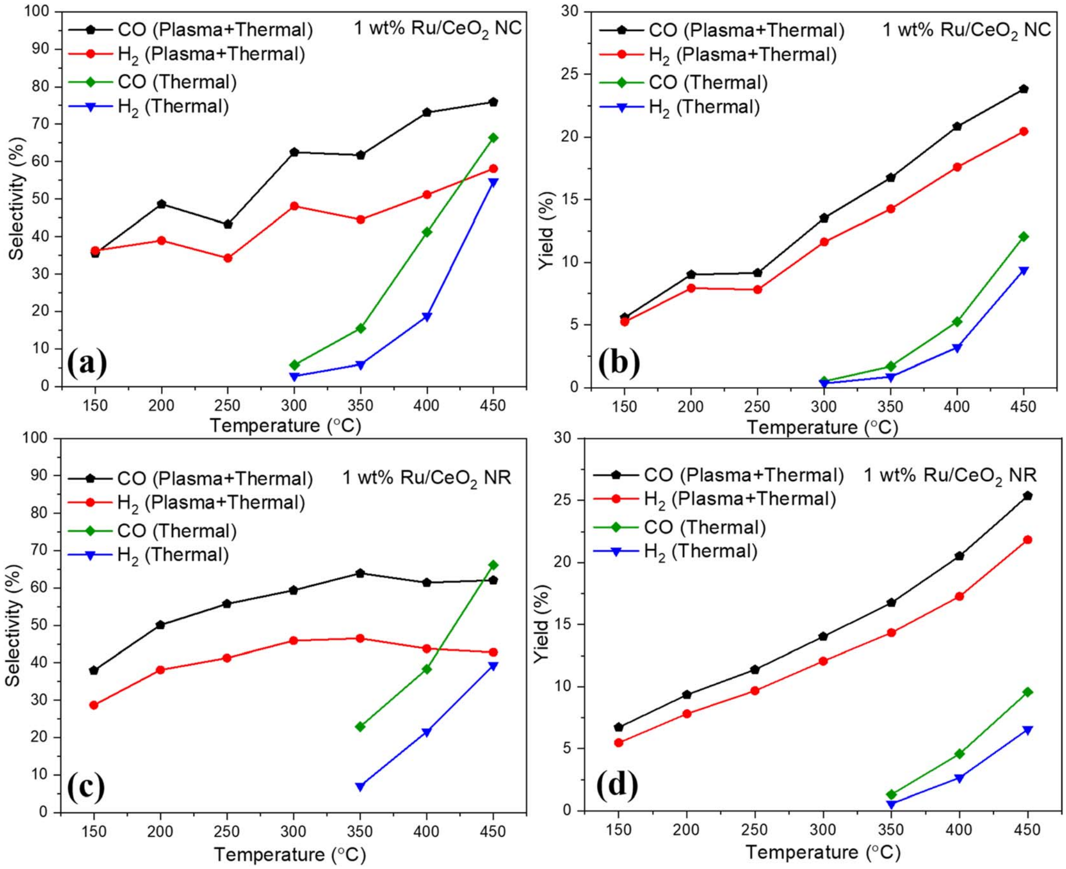

Fig. 11 CO and H_2 (a) selectivity and (b) yield of 1 wt% Ru/CeO_2 NC; (c) selectivity and (d) yield of 1 wt% Ru/CeO_2 NR from 150 °C to 450 °C under thermal and thermal + plasma conditions (catalyst wt: ~200 mg, power: 10.2 to 13.6 W, frequency: 20 kHz, flowrate: CO_2: 250 sccm and CH_4: 100 sccm).

least 250 °C lower than that of thermo-catalytic DRM. Under non-thermal plasma conditions, the collision frequency between electrons and gas molecules increases dramatically, followed by the generation of highly energetic electrons, leading to the generation of more active species such as ions, radicals, *etc.* For instance, the reactant CH_4 can dissociate into CH_x ($x = 0, 1, 2, 3$) species and active H atoms, which are later combined with cracked products from CO_2 and form products such as CO and H_2.[59] The obtained conversion of CH_4 and CO_2 was in the range of ~19% to ~51% and ~17% to ~37%, respectively, for 1 wt% Ru/CeO_2 NR from 150 °C to 450 °C. For 1 wt% Ru/CeO_2 NC, the conversion was ~14% to ~40% for CH_4 and ~16% to ~30% for CO_2. The higher CH_4 conversion than CO_2 conversion may result from CH_4 dissociation reaction and carbon deposition,[60] because excessive coking could happen due to a lack of balance between carbon atoms from CH_4 dissociation and carbon atoms dislodged by active O atoms from CO_2 dissociation. Similarly, Zheng *et al.*[59] reported higher CH_4 conversion than CO_2 at higher discharge power which was consistent with our results. They also reported higher CO selectivity than H_2, and their trend was similar to our results shown in Fig. 11. For plasma-assisted DRM, it is worth mentioning that 1 wt% Ru/CeO_2 NR was more active than 1 wt% Ru/CeO_2 NC. Therefore, the shape and/or exposed crystal planes of the CeO_2 support played a role in DRM. The conversion of CH_4 increased from 40% (1 wt% Ru/CeO_2 NC) to 51% (1 wt% Ru/CeO_2 NR) at 450 °C whereas CO_2 conversion increased from 30% (1 wt% Ru/CeO_2 NC) to 37% (1 wt% Ru/CeO_2 NR) at the same temperature, because CeO_2 NR is predominantly exposed with (110) and (100) or defected (111) facets which can anchor higher content of Ru^{4+} species and provide a greater amount of Ru–O–Ce solid solution, compared to CeO_2 NC. In addition, Ru clusters on the reducible CeO_2 support give rise to partially oxidized Ru, reduced by CeO_2 ($Ru^{\delta+}$–CeO_{2-x}) to provide active chemistry for better conversion selectivity and yield. It is also concluded from the literature that plasma can bring in more basic sites and smaller crystal sizes of catalysts that promote higher reactivity.[61] The catalyst in the plasma zone accelerates the externally applied electric field and creates stronger micro-discharge and surface discharge. A greater number of exciting species can be ruptured from the collisions between highly energetic electrons and reactant molecules which could be adsorbed over the catalysts to achieve the desired products. Based on the carbon balance analysis of the 1 wt% Ru/CeO_2 NR-r catalyst shown in Fig. S8,† it is reflected that approximately 10% deposited carbon was observed from Boudouard or other coking reactions (*i.e.*, CH_4 decomposition). In addition, a very tiny amount of C_2H_6 or ethane was detected using the quantum cascade laser absorption spectroscopy (TDLAS) system, as shown in Fig. S7.† A few possible reasons for this low carbon deposition are: (1) Ru is known for reducing carbon deposition; (2) more CO_2 was supplied than CH_4 during the reaction for enough metastable O ions that can hinder the CH_x recombination and/or can react with the deposited carbon on the catalyst surface; and (3) below 450 °C, CH_4 decomposition is probably preferable, which produces reactive and less stable carbon species. A CH_4 and CO_2 conversion comparison is presented in Fig. S9,† for CeO_2 supports with plasma and under plasma only conditions. Under plasma only conditions, both CH_4 and CO_2 conversions were very low compared to for Ru doped CeO_2 catalysts. The result showed a maximum 3.5% and 5.5% conversion of CH_4 and CO_2, respectively, with the plasma-assisted support and bare plasma. Hence, incorporation of a small amount of Ru dramatically increases the performance. The experimental data on the DRM performance under thermal catalysis and plasma-assisted catalysis using the 1 wt% Ru/SiO_2 catalyst is presented in Fig. S10.†

As shown in Fig. 11, yield and selectivity increased with the temperature increase. The maximum CO selectivity and yield were 75% and 25% for 1 wt% Ru/CeO_2 NC, while for H_2, these were 60% and 22% at 450 °C. The selectivity of CO was better than that of H_2 due to the formation of a hydrocarbon.[62] In addition, at higher temperatures, the selectivity of H_2 tends to diminish due to the enhancement of RWGS reaction.[63,64] Moreover, the side products and carbon deposition play a crucial role in the selectivity and yield of desired products.[65] In a catalytic gas–solid reaction, reactant conversion is inversely proportional to desired product selectivity due to the evolution of secondary gas phase reaction.[66] The produced H_2/CO ratio was less than the unity shown in Fig. 12, which indicates that CO production was higher than H_2 production. This is probably due to the side reactions.[67] RWGS reaction ($CO_2 + H_2 = CO + H_2O$; $\Delta H_{298} = 41$ kj mol^{-1}) is another possible reason for the low H_2/CO ratio, which is a common phenomenon in catalytic DRM.[62] This side reaction can consume the produced H_2, reduce the H_2 yield, and increase CO production. However, the H_2/CO ratio tends to increase gradually with temperature, which indicates that at elevated temperatures, the CeO_2 supported RuO_x catalysts enhanced both DRM and Boudouard reactions given below.[68]

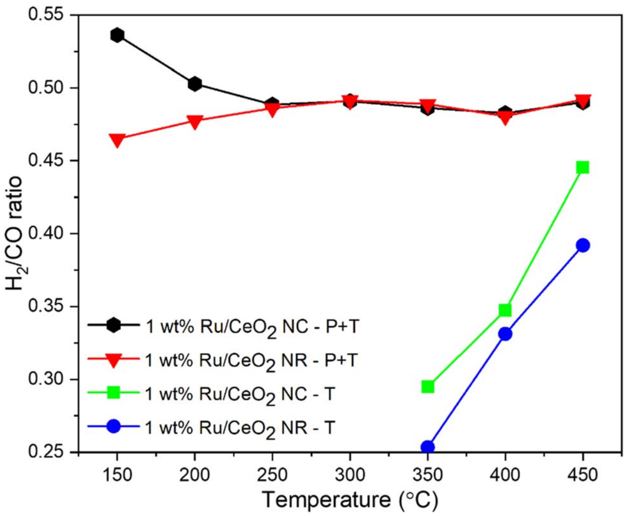

Fig. 12 H_2/CO ratio of 1 wt% Ru/CeO_2 NC and 1 wt% Ru/CeO_2 NR catalysts from 150 °C to 450 °C under thermal and thermal + plasma conditions (catalyst wt: ~200 mg, power: 10.2 to 13.6 W, frequency: 20 kHz, flowrate: CO_2: 250 sccm and CH_4: 100 sccm).

$$2CO = CO_2 + C \tag{9}$$

The addition of RuO_x on CeO_2 supports causes a significant increase in oxygen vacancy concentration due to the interaction of RuO_x and CeO_2 at their interface. For 1 wt% Ru/CeO_2 NR-r the relative oxygen content was 49.5%, calculated from XPS characterization. Sakpal *et al.*[69] reported that 1 wt% Ru/CeO_2 NC promotes a higher concentration of OH and/or carbonate groups and lowers the concentration of oxygen vacancy compared to 1 wt% Ru/CeO_2 NR for CO_2 methanation. On the other hand, exposed (110) and (100) or defected (111) facets by CeO_2 NR have lower oxygen vacancy formation energy and high oxygen vacancy concentration. The interaction of RuO_x species with these CeO_2 facets enhances the activation of CO_2 during the reaction and promotes high catalytic activity in the methane dry reforming reaction.

4.1 Reaction mechanism

For catalytic DRM reaction under thermal-only conditions, it is generally assumed that, for CeO_2 supported Ru catalysts, catalytic DRM is initiated by CH_4 decomposition on active metal Ru sites. At the same time, CO_2 adsorption/dissociation occurs on the support surface.[70] The step-wise CH_4 decomposition leads to $CH_4 \rightarrow CH_3 \rightarrow CH_2 \rightarrow CH$ and C with H_2 production with the following possible surface reactions.

$$2CH_4 + Ru - CeO_2 \rightarrow CeO_2 - Ru^* - CH_3 + CeO_2 - Ru^* - CH_3 + 2H \tag{10}$$

$$2H - Ru^* \rightarrow H_2 + Ru^* \tag{11}$$

On the other hand, CO_2 adsorption on the CeO_2 support leads to either direct dissociation of CO_2 to CO and adsorption of oxygen or formation of the carbonate precursor with further possible reaction routes given in eqn (14) below.

$$CO_2 + Ru - CeO_2 \rightarrow CO_2 - CeO_2^* - Ru \tag{12}$$

$$CO_2 - CeO_2^* \rightarrow CO + O^* - CeO_2^* \tag{13}$$

$$CO_2 - CeO_2^* + O^* \rightarrow CO_3^* - CeO_2^* \tag{14}$$

It should be noted that the produced carbonate precursor is considered a highly reactive intermediate that can promote both CO and H_2 production as well as hydrocarbon formation by interacting with CH_x and spillover H from CH_4 dissociation from the active metal site to the support.

For the plasma-assisted DRM reaction, a possible mechanism can be explained as follows. Plasma and/or high energetic electrons first initiate the activation and dissociation of CO_2 and CH_4, which is followed by the adsorption of intermediate species of CH_x, C, O, H, CO_3^* on the metal and support. This adsorption later leads to numerous reaction routes (Fig. 13).

The dry reforming of methane technique commonly faces the risk of coking or carbon formation at high temperatures mainly either by the methane decomposition (eqn (15): methane cracking) or the Boudouard reaction (eqn (16)). This is because these two reactions are favored at lower temperatures (*i.e.*, 300 °C to 500 °C), which is similar to the furnace (gas) temperature range of 150 °C to 450 °C during the plasma-assisted reactions.

$$CH_4 = 2H_2 + C \tag{15}$$

$$2CO = CO_2 + C \tag{16}$$

Carbon species from the methane decomposition reaction are more reactive than from the Boudouard reaction.[71] According to our experimental temperature range, methane decomposition is highly favored, while Boudouard or other coking reactions are unlikely to occur. The provided carbon balance profile (Fig. S8†) and EDX spectrum (Fig. S11†) of 1 wt% Ru/CeO_2 NR-r catalyst showed approximately 90% that reflects a minimal amount of deposited carbon from Boudouard or other coking reactions and a small amount of C_2H_6 from methane decomposition (Fig. S7†). The production of C-2 species (such as C_2H_2, C_2H_4, C_2H_6) is higher at 150 °C, decreases with increasing reaction temperature, and becomes close to zero when the temperature exceeds 300 °C. The STEM and HRTEM images of the spent 1 wt% Ru/CeO_2 NR catalyst are shown in Fig. S12.† At lower temperatures, the catalyst and plasma synergy produces more CH_3 and CH_2 radicals instead of deposited carbon, and these radicals move the reaction directly to the production of C-2 species. Although methane decomposition promotes amorphous carbon deposition on active RuO_x sites, this was efficiently oxidized by the redox properties of CeO_2 support (Ce^{3+}/Ce^{4+}). The strong metal support interaction of Ru and CeO_2 support formed a solid solution of partially oxidized Ru on reduced CeO_2 support with the chemical formula $Ru^{\delta+}$–CeO_{2-x}. Thus, higher oxygen transfer between Ru and ceria allowed surface carbon gasification and produced CO.

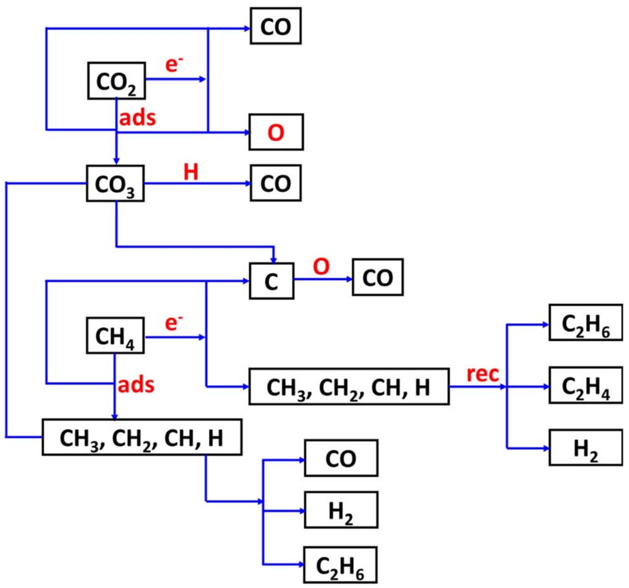

Fig. 13 Possible reaction pathways for the formation of CO, H_2, C_2H_6, and carbon deposition in the direct reforming of CH_4 and CO_2 with DBD.

5. Conclusion

In summary, three different oxides (CeO_2 NR, CeO_2 NC, and SiO_2) supporting 1 wt% Ru catalysts were prepared to study plasma-assisted DRM under non-equilibrium conditions. The reduced 1 wt% Ru/CeO_2 NR showed higher surface basicity and oxygen vacancy concentration and superior low-temperature activity for DRM compared to the 1 wt% Ru/CeO_2 NC and 1 wt% Ru/SiO_2 catalysts. The introduction of non-thermal plasma in a DBD reactor promoted low-temperature DRM conversion over 1 wt% Ru/CeO_2 NR and 1 wt% Ru/CeO_2 NC catalysts compared to the catalyst activity under thermal catalysis only conditions. Compared to 1 wt% Ru/CeO_2 NC-r, the 1 wt% Ru/CeO_2 NR-r catalyst presented 11% higher CH_4 conversion and 7% CO_2 conversion at 450 °C. The enhanced DRM activity with CeO_2 NR as catalyst support is attributed to the highly exposed surface faces and a greater number of surface defects (*i.e.*, Ce^{3+}, oxygen vacancy, and rough surface).

Conflicts of interest

There are no conflicts to declare.

Acknowledgements

This project is supported by the grants from the National Science Foundation (CBET 1856729 and IIP 2044733). We are thankful of Prof. Martin G. Bakker for help with the measurements of the N_2 physisorption isotherms and pore size distribution. This project also received partial financial support from the Alabama Transportation Institute and Alabama Water Institute. The use of electron microscopy facilities at the Alabama Analytical Research Center (AARC) at The University of Alabama is gratefully acknowledged.

References

1 P. Friedlingstein, R. A. Houghton, G. Marland, J. Hackler, T. A. Boden, T. J. Conway, J. G. Canadell, M. R. Raupach, P. Ciais and C. Le Quéré, Update on CO_2 emissions, *Nat. Geosci.*, 2010, **3**, 811–812.

2 Y. Zheng, W. Zhang, Y. Li, J. Chen, B. Yu, J. Wang, L. Zhang and J. Zhang, Energy related CO_2 conversion and utilization: Advanced materials/nanomaterials, reaction mechanisms and technologies, *Nano Energy*, 2017, **40**, 512–539.

3 P. Mehta, P. Barboun, D. B. Go, J. C. Hicks and W. F. Schneider, Catalysis Enabled by Plasma Activation of Strong Chemical Bonds: A Review, *ACS Energy Lett.*, 2019, **4**, 1115–1133.

4 G. A. Olah, A. Goeppert, M. Czaun, T. Mathew, R. B. May and G. K. S. Prakash, Single step bi-reforming and oxidative bi-reforming of methane (natural gas) with steam and carbon dioxide to met gas (CO-2H_2) for methanol synthesis: self-sufficient effective and exclusive oxygenation of methane to methanol with oxygen, *J. Am. Chem. Soc.*, 2015, **137**, 8720–8729.

5 A. Galadima and O. Muraza, Catalytic thermal conversion of CO_2 into fuels: Perspective and challenges, *Renewable Sustainable Energy Rev.*, 2019, **115**, 109333.

6 D. R. Kauffman, J. Thakkar, R. Siva, C. Matranga, P. R. Ohodnicki, C. Zeng and R. Jin, Efficient electrochemical CO_2 conversion powered by renewable energy, *ACS Appl. Mater. Interfaces*, 2015, **7**, 15626–15632.

7 D. Yap, J.-M. Tatibouët and C. Batiot-Dupeyrat, Catalyst assisted by non-thermal plasma in dry reforming of methane at low temperature, *Catal. Today*, 2018, **299**, 263–271.

8 X. Chen, Z. Sheng, S. Murata, S. Zen, H.-H. Kim and T. Nozaki, CH4 dry reforming in fluidized-bed plasma reactor enabling enhanced plasma-catalyst coupling, *J. CO_2 Util.*, 2021, **54**, 101771.

9 J. A. Andersen, J. M. Christensen, M. Østberg, A. Bogaerts and A. D. Jensen, Plasma-Catalytic Dry Reforming of Methane: Screening of Catalytic Materials in a Coaxial Packed-Bed DBD Reactor, *Chem. Eng. J.*, 2020, 125519.

10 M. H. Pham, V. Goujard, J. M. Tatibouët and C. Batiot-Dupeyrat, Activation of methane and carbon dioxide in a dielectric-barrier discharge-plasma reactor to produce hydrocarbons—Influence of La2O3/γ-Al_2O_3 catalyst, *Catal. Today*, 2011, **171**, 67–71.

11 X. Zheng, S. Tan, L. Dong, S. Li and H. Chen, $LaNiO_3$@SiO_2 core–shell nano-particles for the dry reforming of CH_4 in the dielectric barrier discharge plasma, *Int. J. Hydrogen Energy*, 2014, **39**, 11360–11367.

12 H. J. Gallon, X. Tu and J. C. Whitehead, Effects of reactor packing materials on H_2 production by CO_2 reforming of CH_4 in a dielectric barrier discharge, *Plasma Processes Polym.*, 2012, **9**, 90–97.

13 A. H. Khoja, M. Tahir and N. A. S. Amin, Cold plasma dielectric barrier discharge reactor for dry reforming of methane over Ni/γ-Al_2O_3-MgO nanocomposite, *Fuel Process. Technol.*, 2018, **178**, 166–179.

14 M. C. J. Bradford and M. A. Vannice, CO_2 Reforming of CH_4 over Supported Ru Catalysts, *J. Catal.*, 1999, **183**, 69–75.

15 D. Sutton, S. M. Parle and J. R. H. Ross, The CO_2 reforming of the hydrocarbons present in a model gas stream over selected catalysts, *Fuel Process. Technol.*, 2002, **75**, 45–53.

16 D. Qin and J. Lapszewicz, Study of mixed steam and CO_2 reforming of CH_4 to syngas on MgO-supported metals, *Catal. Today*, 1994, **21**, 551–560.

17 J. Wei and E. Iglesia, Reaction pathways and site requirements for the activation and chemical conversion of methane on Ru− based catalysts, *J. Phys. Chem. B*, 2004, **108**, 7253–7262.

18 A. Aitbekova, L. Wu, C. J. Wrasman, A. Boubnov, A. S. Hoffman, E. D. Goodman, S. R. Bare and M. Cargnello, Low-temperature restructuring of CeO_2-supported Ru nanoparticles determines selectivity in CO_2 catalytic reduction, *J. Am. Chem. Soc.*, 2018, **140**, 13736–13745.

19 C. H. Bartholomew, Mechanisms of catalyst deactivation, *Appl. Catal., A*, 2001, **212**, 17–60.

20 P. Ferreira-Aparicio, I. Rodrıguez-Ramos, J. A. Anderson and A. Guerrero-Ruiz, Mechanistic aspects of the dry reforming of methane over ruthenium catalysts, *Appl. Catal., A*, 2000, **202**, 183–196.

21 N. J. Lawrence, J. R. Brewer, L. Wang, T.-S. Wu, J. Wells-Kingsbury, M. M. Ihrig, G. Wang, Y.-L. Soo, W.-N. Mei and C. L. Cheung, Defect engineering in cubic cerium oxide nanostructures for catalytic oxidation, *Nano Lett.*, 2011, **11**, 2666–2671.

22 J. A. Rodríguez and J. Hrbek, Inverse oxide/metal catalysts: a versatile approach for activity tests and mechanistic studies, *Surf. Sci.*, 2010, **604**, 241–244.

23 P. X. Huang, F. Wu, B. L. Zhu, X. P. Gao, H. Y. Zhu, T. Y. Yan, W. P. Huang, S. H. Wu and D. Y. Song, CeO_2 Nanorods and Gold Nanocrystals Supported on CeO_2 Nanorods as Catalyst, *J. Phys. Chem. B*, 2005, **109**, 19169–19174.

24 H.-X. Mai, L.-D. Sun, Y.-W. Zhang, R. Si, W. Feng, H.-P. Zhang, H.-C. Liu and C.-H. Yan, Shape-Selective Synthesis and Oxygen Storage Behavior of Ceria Nanopolyhedra, Nanorods, and Nanocubes, *J. Phys. Chem. B*, 2005, **109**, 24380–24385.

25 C. Ho, J. C. Yu, T. Kwong, A. C. Mak and S. Lai, Morphology-Controllable Synthesis of Mesoporous CeO_2 Nano- and Microstructures, *Chem. Mater.*, 2005, **17**, 4514–4522.

26 Y. Wang, Z. Liu and R. Wang, $NaBH_4$ Surface Modification on CeO_2 Nanorods Supported Transition-Metal Catalysts for Low Temperature CO Oxidation, *ChemCatChem*, 2020, **12**, 4304–4316.

27 Z. Liu, Y. Lu, M. P. Confer, H. Cui, J. Li, Y. Li, Y. Wang, S. C. Street, E. K. Wujcik and R. Wang, Thermally Stable RuO_x–CeO_2 Nanofiber Catalysts for Low-Temperature CO Oxidation, *ACS Appl. Nano Mater.*, 2020, **3**, 8403–8413.

28 S. Agarwal, L. Lefferts, B. L. Mojet, D. A. J. M. Ligthart, E. J. M. Hensen, D. R. G. Mitchell, W. J. Erasmus, B. G. Anderson, E. J. Olivier, J. H. Neethling and A. K. Datye, Exposed Surfaces on Shape-Controlled Ceria Nanoparticles Revealed through AC-TEM and Water–Gas Shift Reactivity, *ChemSusChem*, 2013, **6**, 1898–1906.

29 J. Zhao, Y. He, F. Wang, W. Zheng, C. Huo, X. Liu, H. Jiao, Y. Yang, Y. Li and X. Wen, Suppressing Metal Leaching in a Supported Co/SiO_2 Catalyst with Effective Protectants in the Hydroformylation Reaction, *ACS Catal.*, 2019, **10**, 914–920.

30 R. Wang and R. Dangerfield, Seed-mediated synthesis of shape-controlled CeO_2 nanocrystals, *RSC Adv.*, 2014, **4**, 3615–3620.

31 S. A. Mock, E. T. Zell, S. T. Hossain and R. Wang, Effect of Reduction Treatment on CO Oxidation with CeO_2 Nanorod-Supported CuOx Catalysts, *ChemCatChem*, 2018, **10**, 311–319.

32 J. Li, Z. Liu and R. Wang, Support structure and reduction treatment effects on CO oxidation of SiO_2 nanospheres and CeO_2 nanorods supported ruthenium catalysts, *J. Colloid Interface Sci.*, 2018, **531**, 204–215.

33 M. R. Ahasan, Y. Wang and R. Wang, In situ DRIFTS and CO-TPD studies of CeO2 and SiO2 supported CuOx catalysts for CO oxidation, *Mol. Catal.*, 2022, **518**, 112085.

34 Z. Wei and R. Wang, Chemically etched CeO_2-x nanorods with abundant surface defects as effective cathode additive for trapping lithium polysulfides in Li-S batteries, *J. Colloid Interface Sci.*, 2022, **615**, 527–542.

35 Z. Zhao, *Redox Kinetics Study for Chemical-Looping Combustion, Water and CO_2 Splitting Using Nickel and Cerium-Based Oxygen Carrier*, (2016).

36 Z. Zhao, M. Uddi, N. Tsvetkov, B. Yildiz and A. F. Ghoniem, Redox kinetics study of fuel reduced ceria for chemical-looping water splitting, *J. Phys. Chem. C*, 2016, **120**, 16271–16289.

37 N. A. S. Amin, Co-generation of synthesis gas and C^{2+} hydrocarbons from methane and carbon dioxide in a hybrid catalytic-plasma reactor: A review, *Fuel*, 2006, **85**, 577–592.

38 Y. P. Raizer and J. E. Allen, *Gas Discharge Physics*, Springer, 1991.

39 T. Yabe, K. Mitarai, K. Oshima, S. Ogo and Y. Sekine, Low-temperature dry reforming of methane to produce syngas in an electric field over La-doped Ni/ZrO_2 catalysts, *Fuel Process. Technol.*, 2017, **158**, 96–103.

40 T. Nozaki and K. Okazaki, Non-thermal plasma catalysis of methane: Principles, energy efficiency, and applications, *Catal. Today*, 2013, **211**, 29–38.

41 M. Farahmandjou, M. Zarinkamar and T. P. Firoozabadi, Synthesis of Cerium Oxide (CeO_2) nanoparticles using simple CO-precipitation method, *Rev. Mex. Fis.*, 2016, **62**, 496–499.

42 J. Li, Z. Liu, D. A. Cullen, W. Hu, J. Huang, L. Yao, Z. Peng, P. Liao and R. Wang, Distribution and Valence State of Ru Species on CeO_2 Supports: Support Shape Effect and Its Influence on CO Oxidation, *ACS Catal.*, 2019, **9**, 11088–11103.

43 F. Wang, C. Li, X. Zhang, M. Wei, D. G. Evans and X. Duan, Catalytic behavior of supported Ru nanoparticles on the {1 0 0},{1 1 0}, and {1 1 1} facet of CeO_2, *J. Catal.*, 2015, **329**, 177–186.

44 C. Fernández, C. Pezzotta, G. Raj, E. M. Gaigneaux and P. Ruiz, Understanding the growth of RuO_2 colloidal nanoparticles over a solid support: An atomic force microscopy study, *Catal. Today*, 2016, **259**, 183–191.

45 Y. Wang and R. Wang, Effects of chemical etching and reduction activation of CeO_2 nanorods supported ruthenium catalysts on CO oxidation, *J. Colloid Interface Sci.*, 2022, **613**, 836–846.

46 T. Niu, C. X. Wang, L. H. Zhang and Y. Liu, Potassium promoted Ru/meso-macroporous SiO_2 catalyst for the preferential oxidation of CO in H_2-rich gases, *Int. J. Hydrogen Energy*, 2013, **38**, 7801–7810.

47 C. A. Teles, R. C. Rabelo-Neto, J. R. de Lima, L. V Mattos, D. E. Resasco and F. B. Noronha, The effect of metal type on hydrodeoxygenation of phenol over silica supported catalysts, *Catal. Lett.*, 2016, **146**, 1848–1857.

48 M. A. A. Aziz, A. A. Jalil, S. Wongsakulphasatch and D.-V. N. Vo, Understanding the role of surface basic sites of catalysts in CO_2 activation in dry reforming of methane: a short review, *Catal. Sci. Technol.*, 2020, **10**, 35–45.

49 W. Li, G. Zhang, X. Jiang, Y. Liu, J. Zhu, F. Ding, Z. Liu, X. Guo and C. Song, CO_2 hydrogenation on unpromoted and M-promoted Co/TiO_2 catalysts (M= Zr, K, Cs): effects of crystal phase of supports and metal–support interaction on tuning product distribution, *ACS Catal.*, 2019, **9**, 2739–2751.

50 A. Arman, F. Y. Hagos, A. A. Abdullah, R. Mamat, A. R. A. Aziz and C. K. Cheng, Syngas production through steam and CO_2 reforming of methane over Ni-based catalyst-A Review, in *IOP Conf Ser Mater Sci Eng*, IOP Publishing, 2020, p. 42032.

51 I. Luisetto, S. Tuti, C. Romano, M. Boaro, E. Di Bartolomeo, J. K. Kesavan, S. S. Kumar and K. Selvakumar, Dry reforming of methane over Ni supported on doped CeO2: New insight on the role of dopants for CO2 activation, *J. CO_2 Util.*, 2019, **30**, 63–78.

52 J. Ilsemann, M. M. Murshed, T. M. Gesing, J. Kopyscinski and M. Bäumer, On the support dependency of the CO_2 methanation–decoupling size and support effects, *Catal. Sci. Technol.*, 2021, **11**, 4098–4114.

53 X. Li, D. Li, H. Tian, L. Zeng, Z.-J. Zhao and J. Gong, Dry reforming of methane over Ni/La_2O_3 nanorod catalysts with stabilized Ni nanoparticles, *Appl. Catal., B*, 2017, **202**, 683–694.

54 Z. Ma, S. Zhao, X. Pei, X. Xiong and B. Hu, New insights into the support morphology-dependent ammonia synthesis activity of Ru/CeO_2 catalysts, *Catal. Sci. Technol.*, 2017, **7**, 191–199.

55 H. Huang, Q. Dai and X. Wang, Morphology effect of Ru/CeO_2 catalysts for the catalytic combustion of chlorobenzene, *Appl. Catal., B*, 2014, **158**, 96–105.

56 J. Horlyck, S. Lewis, R. Amal and J. Scott, The impact of La doping on dry reforming Ni-based catalysts loaded on FSP-alumina, *Top. Catal.*, 2018, **61**, 1842–1855.

57 L. He, Y. Ren, Y. Fu, B. Yue, S. C. E. Tsang and H. He, Morphology-dependent catalytic activity of Ru/CeO_2 in dry reforming of methane, *Molecules*, 2019, **24**, 526.

58 Y. Zhou, Y. Li and W. Shen, Shape engineering of oxide nanoparticles for heterogeneous catalysis, *Chem. – Asian J.*, 2016, **11**, 1470–1488.

59 X. Zheng, S. Tan, L. Dong, S. Li and H. Chen, Plasma-assisted catalytic dry reforming of methane: Highly catalytic performance of nickel ferrite nanoparticles embedded in silica, *J. Power Sources*, 2015, **274**, 286–294.

60 S. Hamzehlouia, S. A. Jaffer and J. Chaouki, Microwave Heating-Assisted Catalytic Dry Reforming of Methane to Syngas, *Sci. Rep.*, 2018, **8**, 8940.

61 Y. Ge, T. He, D. Han, G. Li, R. Zhao and J. Wu, Plasma-assisted CO2 methanation: effects on the low-temperature activity of an Ni–Ce catalyst and reaction performance, *R. Soc. Open Sci.*, 2019, **6**, 190750.

62 D. Ray, P. M. K. Reddy and Ch. Subrahmanyam, Ni-Mn/γ-Al_2O_3 assisted plasma dry reforming of methane, *Catal. Today*, 2018, **309**, 212–218.

63 I. Istadi and N. A. Saidina Amin, Co-generation of C_2 hydrocarbons and synthesis gases from methane and carbon dioxide: a thermodynamic analysis, *J. Nat. Gas Chem.*, 2005, **14**, 140–150.

64 H. Tsai and C. Wang, Thermodynamic equilibrium prediction for natural gas dry reforming in thermal plasma reformer, *J. Chin. Inst. Eng.*, 2008, **31**, 891–896.

65 F. Barrai, T. Jackson, N. Whitmore and M. J. Castaldi, The role of carbon deposition on precious metal catalyst activity during dry reforming of biogas, *Catal. Today*, 2007, **129**, 391–396.

66 M. Usman, W. M. A. W. Daud and H. F. Abbas, Dry reforming of methane: Influence of process parameters—A review, *Renewable Sustainable Energy Rev.*, 2015, **45**, 710–744.

67 D. Zambrano, J. Soler, J. Herguido and M. Menéndez, Kinetic study of dry reforming of methane over Ni–Ce/Al_2O_3 catalyst with deactivation, *Top. Catal.*, 2019, **62**, 456–466.

68 J. M. Saad and P. T. Williams, Manipulating the H_2/CO ratio from dry reforming of simulated mixed waste plastics by the addition of steam, *Fuel Process. Technol.*, 2017, **156**, 331–338.

69 T. Sakpal and L. Lefferts, Structure-dependent activity of CeO2 supported Ru catalysts for CO_2 methanation, *J. Catal.*, 2018, **367**, 171–180.

70 M. Li, Z. Sun and Y. H. Hu, Catalysts for CO_2 reforming of CH4: a review, *J. Mater. Chem. A*, 2021, **9**, 12495–12520.

71 A. S. A. S. Omran, *DFT Study of Copper-Nickel (111) Catalyst for Methane Dry Reforming*, 2019.